mater.scichina.com link.springer.com Published online 3 March 2023 | https://doi.org/10.1007/s40843-022-2354-2

Synergistic adsorption and electrocatalytic effect of Mott-Schottky heterostructure-functionalized separator for lithium-sulfur batteries

Jiapei Gu[1], Chenxu Dong[1], Cheng Zhou[1], Chunli Shen[1], Yuqiang Pi[2*] and Xu Xu[1*]

ABSTRACT **The low sulfur usage, strong shuttle effect, and dilatory redox processes limit the practical application of lithium-sulfur batteries (LSBs). The method of separator modification with a unique Mott-Schottky heterostructure used in this work significantly alleviates these issues. This unique structure is synthesized by *in situ* polymerizing the conductive polymer polypyrrole (PPy) on the surface of Bi_2MoO_6 nanosheets to form Bi_2MoO_6-PPy nanosheets. This unique heterostructure can minimize the redox energy barrier on polysulfides due to the strong adsorption effect, high catalytic activity, and built-in electric field of Bi_2MoO_6-PPy nanosheets. The battery demonstrates good cycling stability when assembled with the functional separator modified by Bi_2MoO_6-PPy nanosheets, with an ultralow capacity decay of 0.045% per cycle over 500 cycles at 2 C. Furthermore, even with a high sulfur loading (7.5 mg cm^{-2}), the battery retains an areal capacity of 6.3 mA h cm^{-2} at 0.2 C after 80 cycles. As a result, the suggested Mott-Schottky heterostructure-based Bi_2MoO_6-PPy nanosheets-modified separator (Bi_2MoO_6-PPy@PP separator) successfully suppresses the shuttle effect, providing an effective strategy for deploying efficient LSB.**

Keywords: functionalized separator, lithium-sulfur batteries, Mott-Schottky heterostructures, synergistic effect

INTRODUCTION

To keep up with the rapid growth of mobile electronics, unmanned aerial vehicles, and other technologies, advanced large-scale energy storage systems must continuously increase their energy density, prolong the cycle life, and lower the costs. Lithium-sulfur batteries (LSBs) with high theoretical capacity (1675 mA h g^{-1}), high energy density (2600 W h kg^{-1}), and great cost effectiveness are gaining popularity as an environmentally benign and technologically advanced alternative to lithium-ion batteries (LIBs) [1–3]. However, low real capacity due to the insulated sulfur cathode, and poor cycle life and rate performance due to intermediate dissolution limit the practical uses of LSBs [4–8]. The shuttle effect is especially challenging, because the polysulfide intermediate formed at the cathode dissolves and diffuses to the anode during cycling, resulting in irreversible loss of the active material and lowering the battery life and Coulombic efficiency [9–12]. As a result, suppressing the shuttle effect is a crucial yet difficult technical issue for the practical implementation of LSBs [13–17].

Modifying separators is the most successful method among different measures proposed to solve the shuttle effect of LSBs [18–21]. Carbon materials (graphene, carbon nanotubes, carbon spheres, carbon nanofibers, and conducting polymers) [22], metal compounds (metal oxides, metal sulfides, metal carbides, metal nitrides, and metal phosphorus) [23–26], metal-organic frameworks (MOFs) [27,28], and covalent organic frameworks (COFs) [29] have been reported as modified materials. Carbon compounds, for example, have high electrical conductivity and can physically adsorb polysulfides, but their adsorption capacity is low. The metal compounds have high electrocatalytic activity and a substantial adsorption effect on polysulfides, but their electrical conductivity is modest. Based on the foregoing, the composite structure of these two types of materials may exhibit the benefits of strong adsorption, high catalytic activity, and high conductivity [30–32].

Bismuth molybdate (Bi_2MoO_6) nanosheets have a distinct layered structure that is made of alternate stacking of [Bi_2O_2] and [MoO_4] layers [33–35]. Meanwhile, Bi_2MoO_6 has a strong polar surface and may chemisorb polysulfides as a binary transition metal oxide (BTMO) [36–38]. Bismuth, molybdenum, and oxygen, for example, can form distinct chemical interactions with polysulfides [39–41]. Bi_2MoO_6 nanosheets have mostly been used in visible light-responsive photocatalysis [42,43]. Furthermore, because of their high theoretical capacity, Bi_2MoO_6 nanosheets can be employed as anode materials for LIBs [44,45]. The primary limitation of Bi_2MoO_6 nanosheets is their low electrical conductivity [46,47]. As a result, mixing them with conductive materials boosts the electrochemical performance of Bi_2MoO_6 nanosheets significantly. Polypyrrole (PPy) is a type of conductive polymer with strong electronic conductivity and outstanding mechanical elasticity [48–50]. The strong interaction could substantially reduce polysulfide dissolution, thereby inhibiting the shuttle effect of LSBs.

This paper presents Mott-Schottky-based Bi_2MoO_6-PPy heterostructure nanosheets with dual adsorption and catalytic effects for LSB separator modification. Electrostatic adsorption and *in situ* polymerization were used to modify the conductive polymer PPy on the surface of Bi_2MoO_6 nanosheets, and an n-n-type heterojunction was formed between them. This structure improves the adsorption capacity and redox dynamics of LiPSs

[1] State Key Laboratory of Advanced Technology for Materials Synthesis and Processing, International School of Materials Science and Engineering, Wuhan University of Technology, Wuhan 430070, China
[2] School of Chemistry and Materials Science, Hubei Engineering University, Xiaogan 432000, China
[*] Corresponding authors (emails: xq0502@163.com (Pi Y); xuxu@whut.edu.cn (Xu X))

by utilizing the built-in electric field generated by the accumulation of positive and negative charges on both sides of the heterojunction [51–53]. Theoretical calculations also demonstrate that the Bi_2MoO_6-PPy heterostructure not only has a stronger adsorption impact on polysulfides but may also substantially reduce the energy barrier required for polysulfide conversion. As a result, at high rates, the LSBs with Bi_2MoO_6-PPy@PP separator exhibit high sulfur utilization and outstanding cycling stability. Bi_2MoO_6-PPy heterostructure nanosheets based on Mott-Schottky have the potential to be used in advanced LSBs.

EXPERIMENTAL SECTION

Chemicals and materials

All the chemicals were of analytical grade and were used without further purification. Sodium molybdate dehydrate ($Na_2MoO_4{\cdot}2H_2O$), bismuth (III) nitrate pentahydrate ($Bi(NO_3)_3{\cdot}5H_2O$), and iron trichloride hexahygrate ($FeCl_3{\cdot}6H_2O$) were purchased from Aladdin. Hexadecyl trimethyl ammonium bromide (CTAB) and pyrrole were obtained from Macklin. 1,2-Dimethoxyethane (DME) (99.5%), 1,3-dioxlane (DOL) (99.5%), and Li_2S were purchased from Alfa Aesar.

Preparation of Bi_2MoO_6 nanosheets

A surfactant-assisted one-pot hydrothermal reaction was used to fabricate Bi_2MoO_6 nanosheets. In a typical experiment, 0.260 g of $Na_2MoO_4{\cdot}2H_2O$ and 1.05 g of $Bi(NO_3)_3{\cdot}5H_2O$ were added to 50 mL of deionized water and stirred for 30 min. Next, 0.09 g of CTAB was dissolved in 30 mL of deionized water, which was then added to the above solution and stirred for 30 min. The mixed solution was then placed in a 100-mL stainless steel autoclave coated with Teflon and heated to 140°C for 18 h. Finally, the product was centrifuged and washed several times with deionized water and ethanol before drying at 60°C for 12 h.

Preparation of Bi_2MoO_6-PPy nanosheets

Here, 0.100 g of Bi_2MoO_6 nanosheets were dispersed in 10 mL of deionized water, sonicated for 30 min, and stirred for 2 h. Next, 1 mL of pyrrole was dispersed in 10 mL of deionized water for 30 min and stirred for 2 h to form a homogeneous dispersion, which was then added dropwise to a homogeneous solution of Bi_2MoO_6 nanosheets and stirred for 12 h. Then, 0.040 g of $FeCl_3{\cdot}6H_2O$ was added to the above suspension liquid, while it was continuously magnetically stirred for another 12 h. Finally, centrifugation was used to collect Bi_2MoO_6-PPy nanosheets, which were then rinsed several times with alcohol and deionized water before drying overnight at 60°C.

Preparation of the Bi_2MoO_6-PPy@PP separator

Here, 10 mg of Bi_2MoO_6-PPy nanosheets were ultrasonically dispersed in 60 mL of absolute ethanol for more than 2 h. After standing the homogeneous solution for another 2 h, the supernatant was taken for vacuum filtration on polypropylene (PP) separator to obtain a uniform Bi_2MoO_6-PPy@PP separator. Finally, the Bi_2MoO_6-PPy@PP separator was dried for 8 h at 60°C. The same method was used to synthesize the PP separator modified by Bi_2MoO_6 nanosheets (Bi_2MoO_6@PP). The areal loading of the Bi_2MoO_6 and Bi_2MoO_6-PPy modified layers was set to 0.35 and 0.29 mg cm^{-2}, respectively. The obtained separator was cut into a circular separator with a diameter of 1.7 cm.

Preparation of rGO/S cathode

In 13.3 mL of deionized water, 1.2 mL of graphene dispersion (12.644 mg mL^{-1}) and 0.7 mL of sodium thiosulfate solution (1 mol L^{-1}) were mixed and stirred for 30 min. Next, 6.85 mL of 0.2 mol L^{-1} hydrochloric acid was slowly dropped into the above solution, stirred for 90 min, and centrifuged to collect the solid product, and the volume was adjusted to 14.4 mL with deionized water. 0.76 mL of sodium ascorbate (1 mol L^{-1}) was added to the mixed solution before quickly transferring 1.5 mL of the solution into 10 small glass vials and placing the mixture in a 95°C oven for 2 h to obtain reduced graphene oxide (rGO)/S. It was washed three times with deionized water before being freeze-dried to produce a freestanding rGO/S cathode. For the routine electrochemical performance test, the sulfur content in rGO/S is 60%, and the sulfur loading is 2.5 mg cm^{-2} (Fig. S1). The high sulfur-loaded cathode was created by increasing the amount of sodium thiosulfate solution, and the rGO/S cathodes had high sulfur mass loadings of about 7.5 mg cm^{-2}.

Materials characterizations

The X-ray diffraction (XRD) patterns of crystal structure were recorded using a smart lab diffractometer (Rigaku, Japan) with a Co Kα radiation source (λ = 1.79 Å) at 30 kV and 10 mA. Scanning electron microscopy (SEM) images of the material's structure and morphology were examined using a scanning electron JEOL JSM-7100F microscope (JEOL, Japan). Images of transmission electron microscopy (TEM) were captured using a JEM-2100F/Titan G2 60-300 microscope (JEOL, Japan). A Titan G2 60-300 with an EDS image corrector was used to collect high-resolution TEM (HRTEM) images. A VG MultiLab 2000 instrument was used to collect X-ray photoelectron spectra (XPS). At room temperature, Raman spectra were obtained using a Renishaw Invia Raman spectrometer with a 633-nm excitation laser. A Nicolet 6700 IR spectrometer was used to collect Fourier transform infrared (FT-IR) spectra (Thermo Fisher Scientific Co., USA).

Electrochemical measurement

In an argon gas-filled glovebox, CR2025 coin cells were assembled. Both the water and oxygen levels were less than 0.1 ppm. The as-prepared dry rGO/S samples served as the cathode, while the lithium foil served as the anode. The general separator was Celgard 2500 PP, and the functional separator was Bi_2MoO_6-PPy@PP. The electrolyte was a 1 mol L^{-1} LiTFSI solution in DEM and DOL (1:1 volume ratio) with 0.1 mol L^{-1} $LiNO_3$ as an additive. The electrolyte to S ratio is 15(μL):1(mg), and the Li metal anode had a diameter of 16 mm and a thickness of 600 μm. The galvanostatic charge/discharge cycling and cycling measurements were performed in a multichannel battery testing system (Wuhan LAND Electronic Co., Ltd.) at different current densities in the potential range of 1.7–2.8 V (*vs.* Li/Li$^+$). The cyclic voltammetry (CV) curves and electrochemical impedance spectroscopy (EIS) tests (0.1 Hz–100 kHz, 5 mV) were performed using an electrochemical workstation (Autolab PGSTA T302N).

Ionic conductivity

All the separators were sandwiched between two stainless sheets of steel to be assembled into batteries. The ionic conductivity

was determined using the following equation:

$$\sigma = L / (R_b A), \quad (1)$$

where σ denotes the ionic conductivity (S cm^{-1}), L denotes the thickness of the separator (cm), R_b denotes the resistance (Ω), and A denotes the area of the stainless steel electrode (cm^2).

Lithium-ion diffusion coefficient

The lithium-ion diffusion coefficient was calculated using the Randles-Sevick equation and CV plots of cells with different separators at different scan rates:

$$I_p = 2.69 \times 10^5 n^{1.5} A D_{Li^+}{}^{0.5} C_{Li} v^{0.5}, \quad (2)$$

where I_p denotes the peak current (A), n denotes the charge transfer number, A denotes the area of the cathode (cm^2), D_{Li+} denotes the Li^+ diffusion coefficient, C_{Li^+} denotes the Li^+ concentration (mol L^{-1}), and v denotes the scan rate (V s^{-1}).

Theoretical computations

The Vienna *Ab-initio* Simulation Package with the projector augmented wave method was used to perform the first principle density functional theory (DFT) calculations. To evaluate the immobilization effect of Li_2S_n in Bi_2MoO_6-PPy, the binding energies of Bi_2MoO_6 and Bi_2MoO_6-PPy with Li_2S_n (n = 1, 2, 4, 6, and 8) were computed. The exchange-functional was described by the generalized gradient approximation of the Perdew-Burke-Ernzerhof (PBE) functional. The plane wave cutoff energy was set to 400 eV, and the internal perpendicular forces on each atom were set to be less than 0.05 eV Å^{-1} for the geometry relaxation convergence criterion. Here, 2 × 2 × 1 k-point meshes were used to sample the Brillouin zone integration. The self-consistent calculations used a 10^{-5} eV energy convergence threshold. In the simulation, the DFT-D3 functional was used to account for the physical van der Waals interaction. Finally, the adsorption energies (E_{ads}) were calculated as $E_{ads} = E_{ad/sub} - E_{ad} - E_{sub}$, where $E_{ad/sub}$, E_{ad}, and E_{sub} are the total energies of the optimized adsorbate/substrate system, the adsorbate in the structure, and the clean substrate, respectively. The following equation was used to calculate the free energy:

$$G = E_{ads} + \mathrm{ZPE} - TS, \quad (3)$$

where G, E_{ads}, ZPE, and TS denote the free energy, total energy from DFT calculations, zero-point energy, and entropic contributions, respectively.

RESULTS AND DISCUSSION

Material synthesis and characterization

Fig. 1a depicts the preparation processes for the Bi_2MoO_6@PP/Bi_2MoO_6-PPy@PP separator. First, surfactant-assisted one-pot hydrothermal reactions were employed to synthesize Bi_2MoO_6 nanosheets. Then, using electrostatic adsorption and subsequent *in situ* polymerization, a specific amount of pyrrole monomer was used to generate PPy on the surface of Bi_2MoO_6 nanosheets. Finally, Bi_2MoO_6-PPy nanosheets were assembled into dense stacks on the PP separator using a simple vacuum filtration method. Fig. 1b depicts a schematic of the working mechanism. The Bi_2MoO_6-PPy@PP separator has great potential in the

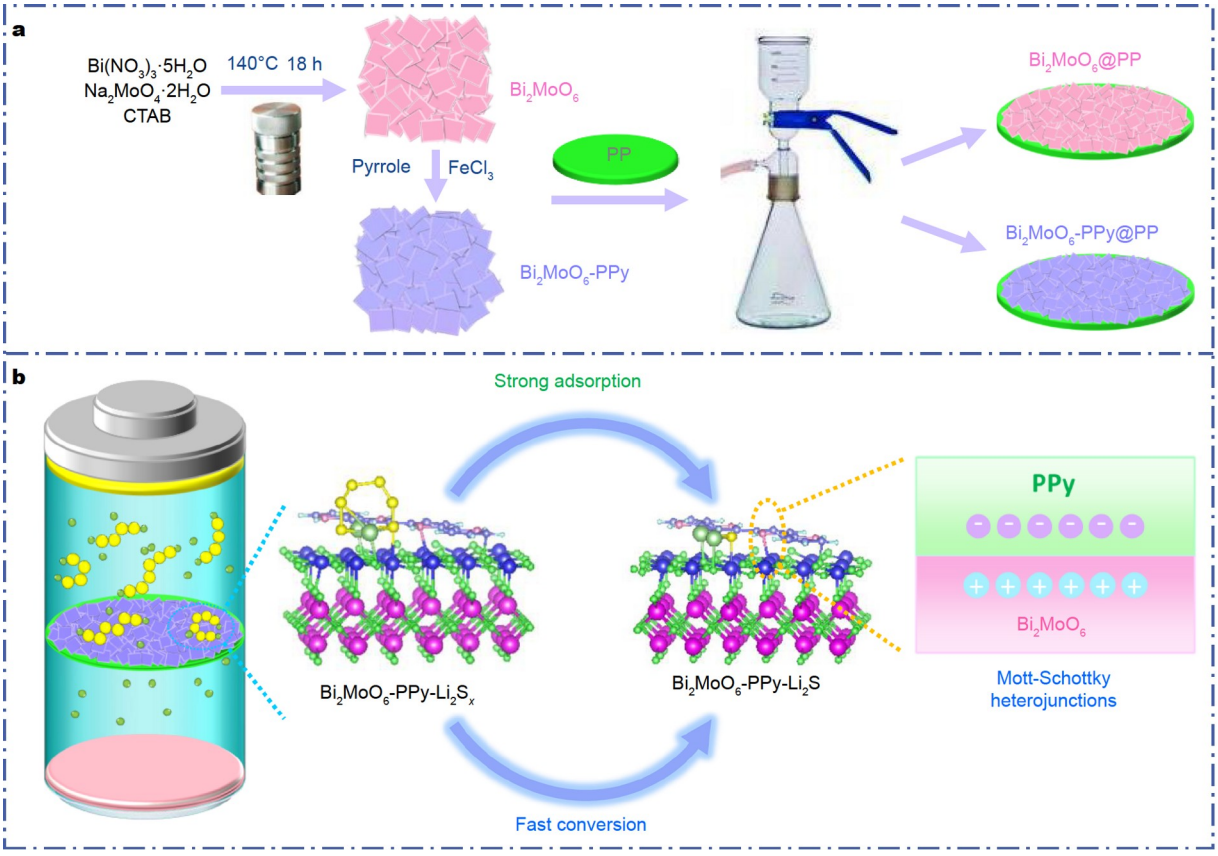

Figure 1 (a) Schematic illustration of the preparation processes of Bi_2MoO_6@PP and Bi_2MoO_6-PPy@PP separator; (b) Bi_2MoO_6-PPy@PP separator for the adsorption and catalysis of polysulfides.

application of LSBs due to the synergistic effect of the strong adsorption of polysulfides by PPy as a conductive polymer and the fast catalysis of polysulfides by Bi_2MoO_6 as BTMO, as well as the unique Mott-Schottky heterogeneous layer structure of Bi_2MoO_6-PPy.

SEM and HRTEM images were used to examine the morphologies of Bi_2MoO_6 and Bi_2MoO_6-PPy nanosheets. The pristine two-dimensional Bi_2MoO_6 nanosheets with uniform size were prepared using the surfactant-assisted method, as shown in the SEM images (Fig. S2a). Fig. 2a shows an SEM image of Bi_2MoO_6-PPy nanosheets obtained after PPy modification. The modified nanosheets retain a two-dimensional nanosheet structure similar to the pristine Bi_2MoO_6. HRTEM images confirm the sheet-like structure of Bi_2MoO_6 and Bi_2MoO_6-PPy nanosheets with an average diameter of 60–80 nm (Fig. S2b and Fig. 2b). The uniform PPy modification layer has a thickness of about 4 nm, as shown in Fig. 2c. Bi_2MoO_6 nanosheets also have a lattice stripe with a layer spacing of 0.273 nm corresponding to the (002) plane (Fig. S2f). The surface modification with PPy has no effect on the overall crystal structure of the Bi_2MoO_6 nanosheets, as shown in Fig. 2d. Here, the characteristic crystal planes of Bi_2MoO_6 nanosheets were still observed, while the amorphous structure of PPy has no specific lattice *d*-spacing. According to the elemental mapping, Bi, O, and Mo elements are distributed uniformly in Bi_2MoO_6 nanosheets (Fig. S2c–e). Bi, O, Mo, and N elements are evenly distributed throughout the Bi_2MoO_6-PPy nanosheets (Fig. 2e–h). Fast electron transfer is enabled by the heterointerface contact formed between Bi_2MoO_6 and PPy. The PPy mass content is 17 wt% as determined by thermogravimetric analysis (TGA, Fig. S3).

XRD patterns were used to determine the phase purity and crystal structure of the prepared Bi_2MoO_6 and Bi_2MoO_6-PPy nanosheets. As illustrated in Fig. 2i, Bi_2MoO_6 diffraction peaks can be seen at 11.0°, 28.3°, 32.7°, 47.1°, 55.7°, and 58.6°, which correspond to the orthogonal phase Bi_2MoO_6 diffraction planes (020), (131), (002), (260), (133), and (262) (JCPDS No. 21-0102). The XRD pattern of Bi_2MoO_6-PPy is identical to that of Bi_2MoO_6, confirming the amorphous structure of PPy. This indicates that the addition of PPy has no discernible effect on the crystal structure of Bi_2MoO_6. The structure of the as-prepared samples was then examined using Raman spectroscopy (Fig. 2j). The bending motion of MoO_6 octahedra and BiO_3 tetrahedra is represented by the Raman bands at 285, 350, and 402 cm^{-1}. The stretching vibrations of the twisted MoO_6 octahedra in the γ-Bi_2MoO_6 structure are responsible for the bands at 719, 801, and 843 cm^{-1}. The 900–1600 cm^{-1} wavenumber range, which corresponds to the vibrational modes of PPy, distinguishes well-defined phonon modes, confirming the formation of Bi_2MoO_6-PPy. Two small peaks at 970 and 1359 cm^{-1} correspond to the PPy characteristic peaks, while the typical peaks at 1560 and 1051 cm^{-1} are attributed to the C=C stretching vibration and the C–H in-plane deformation vibration in pure PPy, respectively. Fig. 2k depicts the FT-IR spectra of Bi_2MoO_6 and Bi_2MoO_6-PPy nanosheets. The strong bands at 562, 728, and 847 cm^{-1} in pristine Bi_2MoO_6 samples are attributed to the stretching modes of Bi–O, Mo–O, or M–O–Mo groups. The FT-IR spectra of

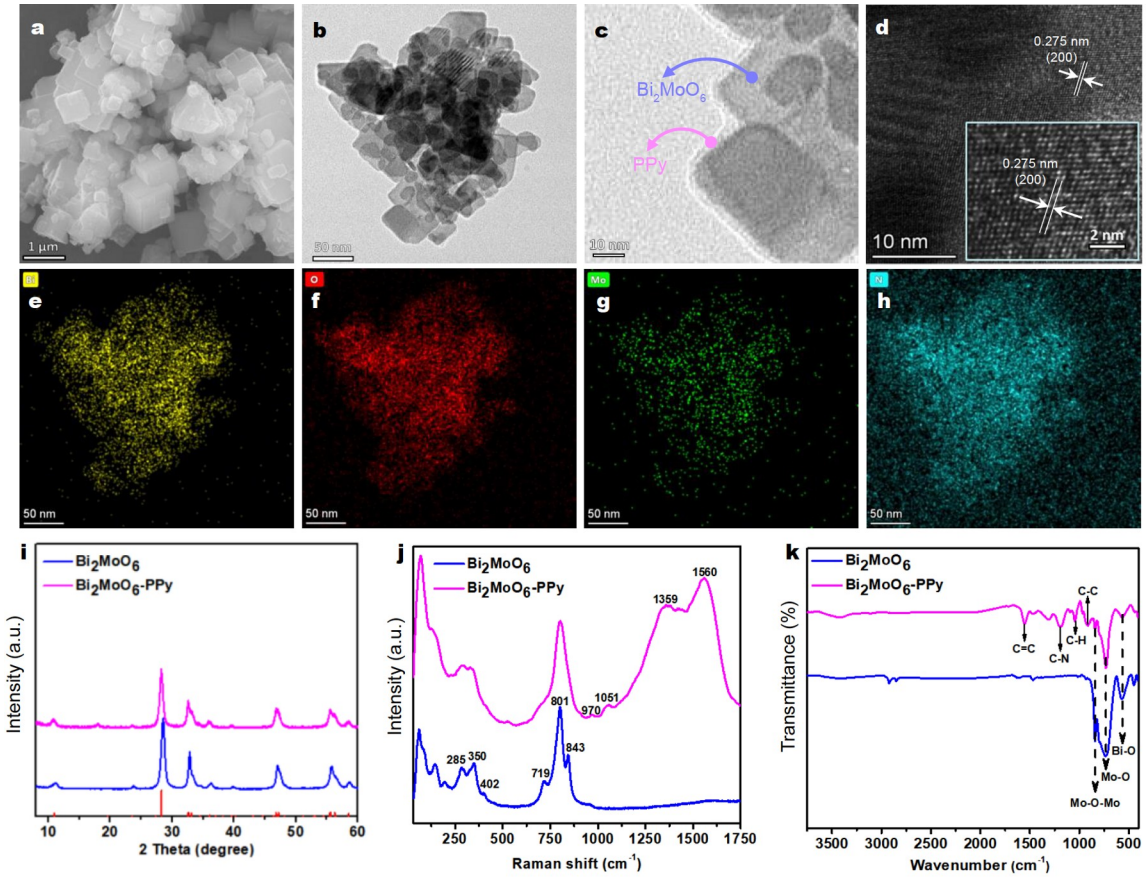

Figure 2 (a) SEM image; (b–d) various magnification TEM images; (e–h) TEM elemental mapping images of Bi, O, Mo, and N of Bi_2MoO_6-PPy nanosheets. (i) XRD patterns, (j) Raman spectra, and (k) FT-IR spectra of Bi_2MoO_6 and Bi_2MoO_6-PPy.

Bi_2MoO_6-PPy nanosheets reveal PPy-specific peaks.

Furthermore, the chemical state and surface elemental composition of the specimen were assessed using XPS spectroscopy (Fig. S4). The full measured spectra in Fig. S4a show the presence of Bi, Mo, O, and N over a wide energy range. The characteristic peaks at 164.2 and 158.8 eV (Fig. S4b) correspond to Bi $4f_{5/2}$ and Bi $4f_{7/2}$, respectively, indicating the presence of Bi in its trivalent oxidation state. The peaks at 235.3 and 232.1 eV (Fig. S4c) are attributed to Mo $3d_{3/2}$ and Mo $3d_{5/2}$ for Mo^{6+}, respectively, and the peaks at 529.2, 529.9, and 530.9 eV (Fig. S4d) are attributed to the presence of oxygen in the sample. The N 1s peak of Bi_2MoO_6-PPy at 398.7 eV in Fig. S4e further demonstrates the successful modification of PPy. Furthermore, the Bi_2MoO_6-PPy binding energies were all shifted toward higher binding energies (Fig. S4b–d), which is attributed to the strong chemical interaction between Bi_2MoO_6 nanosheets and PPy. The successful preparation of Bi_2MoO_6 and Bi_2MoO_6-PPy nanosheets was further confirmed by XRD, Raman, FT-IR, and XPS analysis.

Table S1 shows the surface area and pore structure of Bi_2MoO_6 and Bi_2MoO_6-PPy. The specific surface areas of Brunauer-Emmett-Teller (BET) are 22.59 and 29.04 $m^2 g^{-1}$, respectively. The contact area of Bi_2MoO_6-PPy is slightly larger than that of Bi_2MoO_6. The pore volume decreases from 0.17 to 0.09 $cm^3 g^{-1}$ after loading PPy on the surface of Bi_2MoO_6 nanosheets, indicating that PPy effectively reduces nanosheet agglomeration. Meanwhile, Fig. S5 demonstrates that the N_2 adsorption and desorption curves of Bi_2MoO_6 and Bi_2MoO_6-PPy are type IV isotherms, which are typical of mesoporous materials. As a result, the mesoporous structure and large surface area containing conductive polymers allow for easy electron transfer and sufficient polysulfide adsorption sites. Furthermore, the four-probe method was used to measure the electrical conductivity of Bi_2MoO_6-PPy (141.9 S cm^{-1}), which is significantly higher than that of Bi_2MoO_6 (< 0.075 S cm^{-1}). The modification of the conductive polymer PPy improves the electronic conductivity of the nanosheets as well.

Separator characterization

The functional separators were fabricated using a facile and scalable method of vacuum filtration of Bi_2MoO_6 and Bi_2MoO_6-PPy nanosheets dispersed in ethanol. The surface of Bi_2MoO_6@PP and Bi_2MoO_6-PPy@PP separators had a uniform and dense morphology when compared with the porous surface of PP separator (Fig. S6a, b and Fig. 3a). The thicknesses of the Bi_2MoO_6 and Bi_2MoO_6-PPy nanosheets-modified layers were approximately 15 and 12 μm, respectively, as shown in the cross-sectional SEM images (Fig. S6c and Fig. 3b). Tensile tests were performed on three different separators to further validate the mechanical toughness of the modified separators. The displacement of the Bi_2MoO_6-PPy@PP separator is much larger than that of PP separator, as shown in the stress-strain curves (Fig. 3c), indicating that the modified separator has better tensile resistance and mechanical properties. Thermal stability is critical for increasing the safety of LSBs. PP, Bi_2MoO_6@PP, and Bi_2MoO_6-PPy@PP separators were all treated for 1 h at 120°C. The shape and surface color of Bi_2MoO_6@PP and Bi_2MoO_6-PPy@PP separators did not change after 1-h heating when compared with the curled PP separator, as shown in Fig. 3d, indicating that the thermal stability of the modified separator

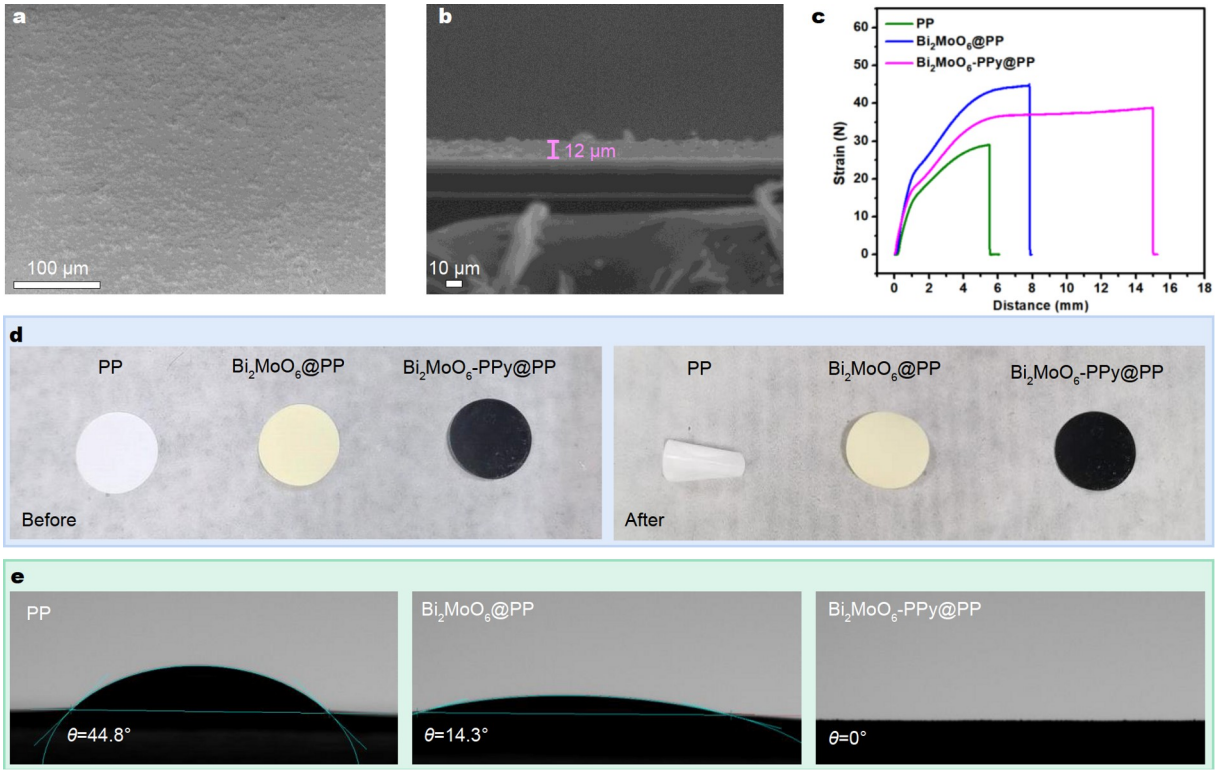

Figure 3 (a) SEM image of the surface and (b) the cross-sectional SEM image of Bi_2MoO_6-PPy@PP separator; (c) stress-strain curves of PP, Bi_2MoO_6@PP, and Bi_2MoO_6-PPy@PP separators; (d) digital photographs of PP, Bi_2MoO_6@PP, and Bi_2MoO_6-PPy@PP separators before and after thermal treatment at 120°C for 1 h; (e) static contact angle measurements with electrolyte for PP, Bi_2MoO_6@PP, and Bi_2MoO_6-PPy@PP separators.

was significantly improved. Furthermore, we folded and curled Bi_2MoO_6-PPy-modified separator numerous times to ensure the mechanical integrity of the modification layer. As shown in Fig. S7, the modified Bi_2MoO_6-PPy@PP separator recovered its initial state without breaking or peeling, indicating that the modification layer firmly adhered to the PP separator. The static contact angle test can be used to determine the wettability of the separator to the electrolyte. The contact angle of the electrolyte on the surface of the pristine PP separator is approximately 44.8°. The contact angle on the surface of Bi_2MoO_6@PP separator is approximately 14.3°. In contrast, when the electrolyte drops on the surface of Bi_2MoO_6-PPy@PP separator, it immediately diffuses completely. Its contact angle is approximately 0°, as shown in Fig. 3e. It is demonstrated that Bi_2MoO_6-PPy@PP separator has excellent electrolyte wettability. The effect of different separators on polysulfide trapping was investigated using permeation tests on a double-L device, as shown in Fig. S8. Separators of pristine PP, Bi_2MoO_6@PP, and Bi_2MoO_6-PPy@PP separated the Li_2S_6 solution and the blank electrolyte on both sides. It is clear that heavy polysulfide diffusion occurred over time in the device with the pristine PP separator, and the Bi_2MoO_6@PP separator also showed a small amount of polysulfide penetration after 12 h, whereas the blank electrolyte in the device with the Bi_2MoO_6-PPy@PP separator was barely penetrated by polysulfides even after 12 h. The results show that Bi_2MoO_6-PPy@PP separator has a strong synergistic effect on polysulfides in terms of physical adsorption and chemical limitation. Furthermore, the Li^+ transport capacity of the pristine PP, Bi_2MoO_6@PP, and Bi_2MoO_6-PPy@PP separators was evaluated using EIS measurements (Fig. S9a). The Li^+ conductivity of Bi_2MoO_6-PPy@PP separator is 0.6738 mS cm^{-1}, which is higher than that of PP (0.1631 mS cm^{-1}) and Bi_2MoO_6@PP (0.5666 mS cm^{-1}), indicating that Bi_2MoO_6-PPy@PP separator reduces the Li-ion diffusion barrier and improves Li^+ transport capability (Fig. S9b).

Electrochemical performance

The Mott-Schottky analysis is widely used for determining the semiconductor type (n- or p-type) [54–56]. As shown in Fig. 4a, the Mott-Schottky curves of Bi_2MoO_6 and Bi_2MoO_6-PPy both

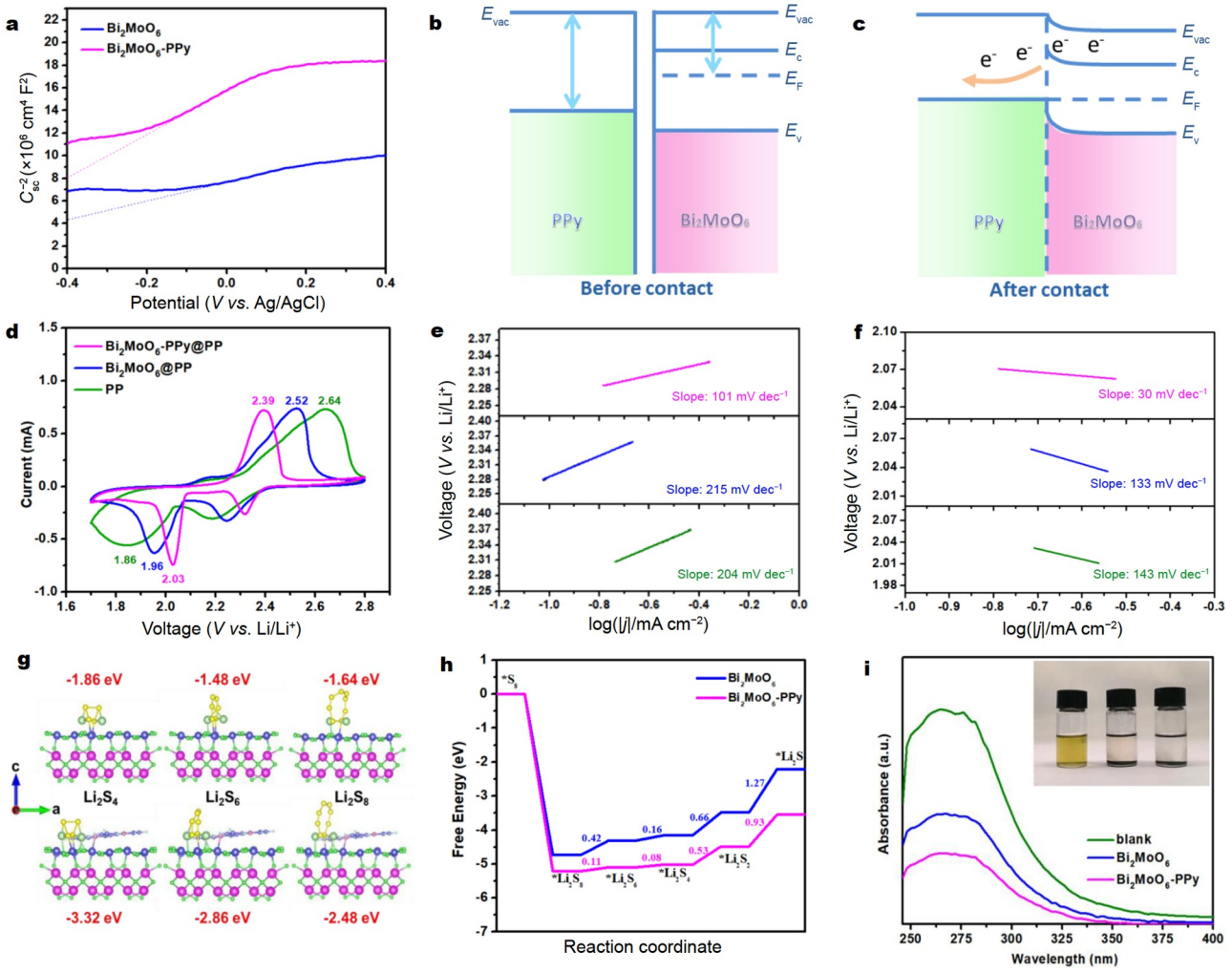

Figure 4 (a) Mott-Schottky plots of Bi_2MoO_6 and Bi_2MoO_6-PPy; (b, c) schematic illustration of the Mott-Schottky-type contact of Bi_2MoO_6-PPy before and after contact; (d) CV curves; (e, f) Tafel slopes from the cathodic peaks of the CV curves; (g) optimized configurations for the binding of long-chain Li_2S_x to Bi_2MoO_6 and Bi_2MoO_6-PPy; (h) energy profiles for the reduction of LiPSs on Bi_2MoO_6 and Bi_2MoO_6-PPy substrates; (i) UV-vis absorption spectra and optical image of the blank Li_2S_6 solution and Li_2S_6 solutions with the addition of Bi_2MoO_6 and Bi_2MoO_6-PPy for 24 h at room temperature. The inset shows the color comparison of the solutions.

have positive slopes, indicating that Bi_2MoO_6 is a typical n-type semiconductor and that when an n-n-type heterojunction is formed between Bi_2MoO_6 and PPy in Bi_2MoO_6-PPy, the Mott-Schottky heterostructure can effectively promote the catalytic conversion of LiPSs [57]. The possible mechanism of the Bi_2MoO_6-PPy heterostructure before and after contact is simulated in Fig. 4b, c. The work functions of Bi_2MoO_6 and PPy were calculated to be 3.93 and 4.36 eV, respectively, based on the results of ultraviolet photoelectron spectroscopy (Fig. S10). As a result of the potential difference, electrons in the semiconductor Bi_2MoO_6 with a low work function will spontaneously transfer to PPy through the interface until the system reaches the same Fermi energy level equilibrium. At the Bi_2MoO_6/PPy heterointerface, PPy will spontaneously induce an electric field directed toward the semiconductor Bi_2MoO_6, causing charge redistribution. The resulting built-in electric field allows polysulfide anions, once adsorbed on PPy, to more easily migrate to the positively charged Bi_2MoO_6 side, promoting polysulfide catalytic conversion. Furthermore, the built-in electric field-induced charge redistribution accelerates electron transport and Li-ion diffusion, improving the kinetics of electrochemical reactions. Because of the built-in electric field generated by the accumulation of positive and negative charges on the Bi_2MoO_6 side and the PPy side, respectively, this structure is beneficial in the LSB system to enhance LiPS binding capacity and redox kinetics.

CR2025 coin cells with freestanding rGO/S composite cathodes were assembled to evaluate the electrochemical performance of the modified separators. The modified separators' catalytic ability for the redox of LiPSs was first investigated using CV testing of coin cells assembled with PP, Bi_2MoO_6@PP, and Bi_2MoO_6-PPy@PP separators. The two cathodic peaks of the battery based on Bi_2MoO_6-PPy@PP separator are located at 2.32 and 2.03 V, respectively, as shown in Fig. 4d, and are attributed to the formation of S_8 to long-chain polysulfides to solid Li_2S_2 and Li_2S. The anodic peak at 2.39 V can be attributed to the conversion of solid-state Li_2S_2 and Li_2S to long-chain polysulfides to S_8, and it is lower than that of the cell assembled with PP (2.52 V) and Bi_2MoO_6@PP (2.64 V). The battery with Bi_2MoO_6-PPy@PP separator, on the other hand, showed a smaller potential gap in the redox peak and higher current density, indicating that the presence of n-n-type heterojunction in Bi_2MoO_6-PPy can accelerate the polysulfides redox kinetics to improve sulfur utilization. Furthermore, as shown in Fig. 4e, f, the Tafel slopes of cells assembled with different separators were obtained by fitting the cathode peaks. Bi_2MoO_6-PPy@PP separators have lower Tafel slopes than PP and Bi_2MoO_6@PP separators, demonstrating that the Bi_2MoO_6-PPy-modified separator effectively accelerates the redox reaction kinetics of LiPSs. To investigate the Li^+ diffusion coefficient, the CV curves of the LSBs with pristine PP, Bi_2MoO_6@PP, and Bi_2MoO_6-PPy@PP separators were measured at scan rates of 0.1–0.4 mV s^{-1} (Fig. S11a–c), as well as the corresponding linear relation of peak current (I_p) *versus* the square root of scan rate. The fitted slopes of the peak current *vs.* square root of the scan rate lines at different redox peaks, according to the Randles-Sevick equation, positively reflect the L^+ diffusion coefficient. Bi_2MoO_6-PPy@PP separator has a much higher L^+ diffusion coefficient than Bi_2MoO_6@PP and PP separators at all redox states (peaks 1, 2, and 3), implying accelerated Li^+ diffusion behaviors and LiPS kinetics conversion (Fig. S11d–f).

The CV curves of the symmetric cells were also used to evaluate the catalytic ability of different separators (Fig. S12), and the current response of the symmetric cells with Bi_2MoO_6-PPy@PP separators was significantly higher than that of PP separators, demonstrating that the sulfur utilization rate and redox kinetics were significantly improved. The charge transfer resistance (R_{ct}) of cells with Bi_2MoO_6-PPy@PP separator (18.1 Ω) is much smaller than that of Bi_2MoO_6@PP (60.5 Ω) and PP separator (94.1 Ω), indicating that Bi_2MoO_6-PPy can accelerate kinetic redox reactions for the catalytic conversion of LiPSs (Fig. S13a). In addition, linear sweep voltammetry (LSV) was used to assess the electrochemical stability and electrocatalytic activity of various separators (Fig. S13b). Bi_2MoO_6-PPy exhibits excellent electrochemical stability as well as a higher current response. According to the findings, Bi_2MoO_6-PPy effectively accelerates the redox reaction kinetics of LiPSs.

DFT calculations confirmed the novel structure's synergistic adsorption-electrocatalytic effect. First, in Fig. 4g and Fig. S14, the optimized geometric models of long-chain Li_2S_x binding to Bi_2MoO_6 and Bi_2MoO_6-PPy are shown, and the calculated binding energies are shown in Fig. S15. Bi_2MoO_6 has binding energies of −1.86, −1.48, and −1.64 eV to Li_2S_4, Li_2S_6, and Li_2S_8, respectively, while Bi_2MoO_6-PPy has binding energies of −3.32, −2.86, and −2.48 eV. The results show that the separator modified by the Bi_2MoO_6-PPy heterojunction has a higher polysulfide adsorption capacity. The calculated Gibbs free energies required for the conversion of each polysulfide by Bi_2MoO_6 and Bi_2MoO_6-PPy are also shown in Fig. 4h. As previously stated, the conversion from Li_2S_2 to Li_2S is the rate-limiting step in the entire process. The Gibbs free energy of Li_2S formation on Bi_2MoO_6-PPy is 0.93 eV, which is lower than the Gibbs free energy of Bi_2MoO_6 (1.27 eV). Furthermore, the Gibbs free energy of Bi_2MoO_6-PPy is lower than that of Bi_2MoO_6 during the transformation process, demonstrating that the heterogeneous structure of Bi_2MoO_6-PPy has a better catalytic effect in promoting polysulfide conversion. In addition, to demonstrate the superiority of the Bi_2MoO_6-PPy heterostructure for LiPS adsorption, we added equal masses (5 mg) of Bi_2MoO_6 and Bi_2MoO_6-PPy to 3 mL of Li_2S_6 solution (2 mmol L^{-1}) for visual static adsorption tests. After 24 h of adsorption at room temperature, the color of the supernatant of Bi_2MoO_6-PPy becomes almost colorless (Fig. 4i, inset). After adsorption, the ultraviolet-visible (UV-vis) absorption spectra of the supernatant were measured (Fig. 4i), and the blank group showed Li_2S_6 characteristic peaks between 250 and 300 nm, whereas Bi_2MoO_6 and Bi_2MoO_6-PPy showed weaker absorption peaks, indicating that Bi_2MoO_6-PPy has more effective anchoring ability for LiPSs. Furthermore, XPS measurements of Bi_2MoO_6-PPy were performed before and after the adsorption test to further investigate the chemical interaction between the Bi_2MoO_6-PPy and the polysulfides. As shown in Fig. S16a, b, Bi_2MoO_6-PPy nanosheets have two typical Bi $4f_{5/2}$ (164.2 eV) and Bi $4f_{7/2}$ (158.8 eV) peaks for Bi and two typical Mo $3d_{3/2}$ (235.3 eV) and Mo $3d_{5/2}$ (232.1 eV) peaks for Mo^{6+}, which obviously shift toward lower binding energies after anchoring the Li_2S_6. The electron transfer from negatively charged LiPSs to positively charged Mo ions is primarily responsible for this, indicating a strong interaction between the polysulfides and Bi_2MoO_6-PPy. Notably, typical S 2p and Li 1s peaks appear following Li_2S_6 adsorption (Fig. S16c, d). These findings clearly show that Bi_2MoO_6-PPy has a strong chemical effect on LiPSs, which can effectively suppress the shuttle effect in LSBs.

After confirming the benefits of the Bi_2MoO_6-PPy heterostructure in LSBs, the electrochemical performance was assessed. Fig. 5a depicts the cycling performance of LSBs with PP, Bi_2MoO_6@PP, and Bi_2MoO_6-PPy@PP separators at 0.5 C. Because of the high catalytic activity of Bi_2MoO_6 nanosheets, Bi_2MoO_6@PP and Bi_2MoO_6-PPy@PP separators have higher capacity in the initial stage, and the high capacity retention rate after 100 cycles indicates that the modified separator has higher adsorption and catalytic efficiency. Fig. 5b depicts the initial charge/discharge curves of cells assembled with PP and Bi_2MoO_6-PPy@PP separators at 0.2 C. The Bi_2MoO_6-PPy@PP separator battery also has a lower polarization potential than the PP separator battery. Fig. 5c depicts the rate performance of batteries with various separators. The highest discharge capacities of Bi_2MoO_6-PPy@PP separator were 1635, 1130, 979, 813, and 666 mA h g^{-1} at 0.2, 0.5, 1, 2, and 3 C, respectively, and when the current rate was reduced to 0.2 C, the discharge capacity recovered to 1068 mA h g^{-1}, indicating good rate performance. The conversion of LiPSs catalyzed by Bi_2MoO_6-PPy heterostructure accounts for the excellent rate capability of Bi_2MoO_6-PPy@PP. Fig. 5d and Fig. S17 show the charge/discharge curves at various current rates, and the polarization voltage of the separators increases significantly with increasing current density. The Bi_2MoO_6-PPy@PP separator has a lower polarization voltage (Fig. 5e) and a higher QL (quantity of charge of the long-plateau) ratio, especially at high rates (Fig. 5f). The results show that Bi_2MoO_6-PPy@PP separator can capture and transform polysulfides effectively. To confirm the long-term cycling performance of batteries assembled with various separators, 500 cycles at 2 C were tested (Fig. 5g). The battery assembled with Bi_2MoO_6-PPy@PP separator demonstrates an initial discharge capacity of 773 mA h g^{-1}, which is significantly higher than those with PP separator (137 mA h g^{-1}) and Bi_2MoO_6@PP separator (445 mA h g^{-1}). The capacity remains around 596 mA h g^{-1} after 500 cycles, and the capacity decay rate per cycle is only 0.045%, which is lower than those of most functionalized-based PP separators (results are shown in Table S2). In the commercial application of LSBs, sulfur areal loading is an important indicator. As a result, we evaluated the battery performance of various separators at a high sulfur loading of 7.5 mg cm^{-2}. As illustrated in Fig. 5h, the battery with Bi_2MoO_6-PPy@PP separator demonstrates an initial discharge capacity of 1121 mA h g^{-1} (8.4 mA h cm^{-2}) at 0.2 C and remains at 839 mA h g^{-1} (6.3 mA h cm^{-2}) after 80 cycles, which is sig-

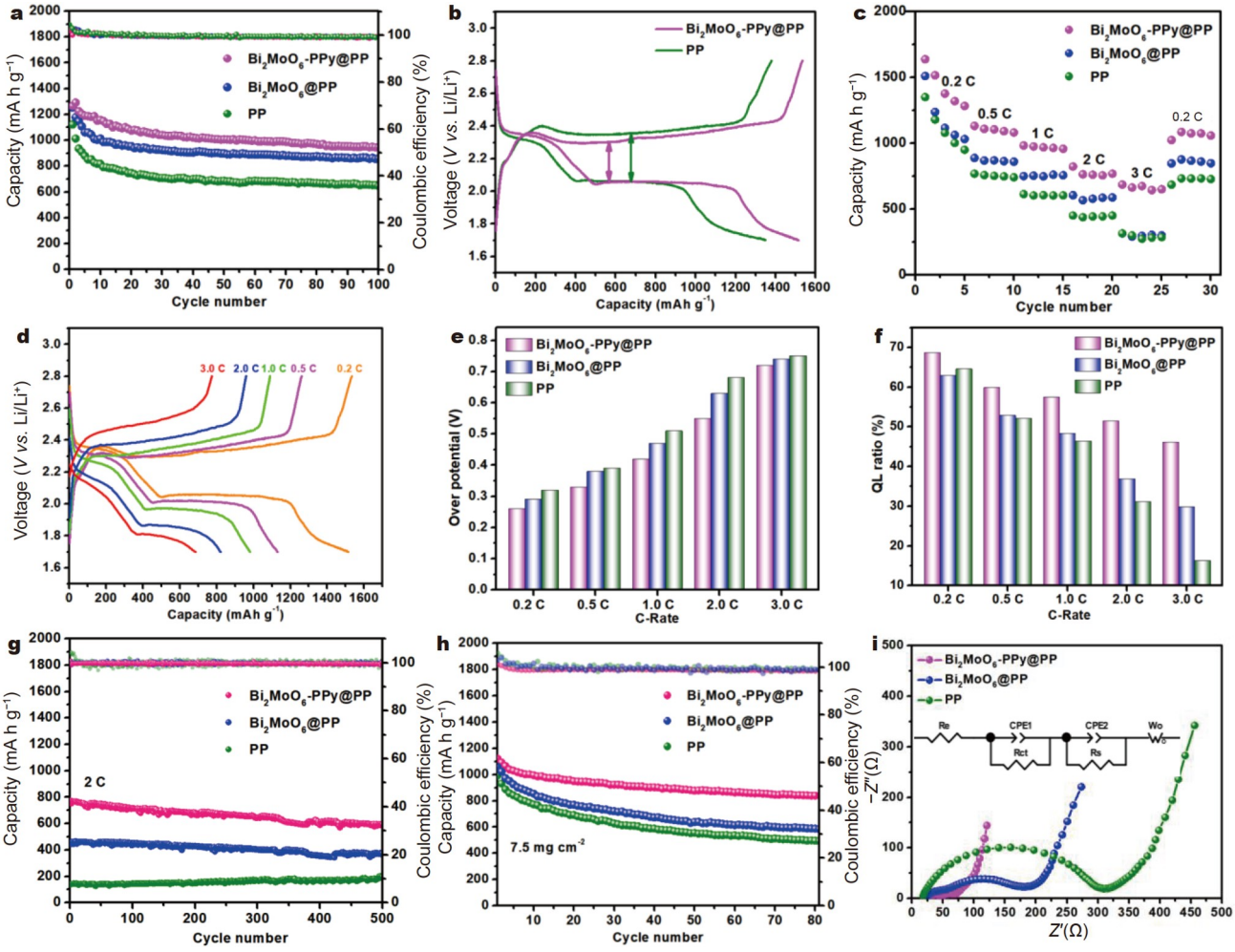

Figure 5 Electrochemical performance of the LSBs with different separators. (a) Cycling test at 0.5 C; (b) galvanostatic charge-discharge profiles at 0.2 C in the potential window from 1.7 to 2.8 V; (c) rate performance; (d) galvanostatic charge-discharge profiles of the LSBs with Bi_2MoO_6-PPy@PP separator at different rates; (e, f) overpotentials and QL ratios at different rates; (g) long-term performance at a current density of 2 C; (h) cycling stability under a high sulfur loading; (i) EIS test.

nificantly higher than those of the batteries with Bi_2MoO_6@PP and PP separators, indicating that Bi_2MoO_6-PPy@PP separator can effectively suppress the shuttle effect of LiPSs even when sulfur levels are high. The results of EIS (Fig. 5i) reveal that the battery assembled with Bi_2MoO_6-PPy@PP separator has a low charge transfer resistance due to its high catalytic ability and fast charge transfer kinetics.

Furthermore, after cycling at 2 C with a PP separator, the surface of the Li anode for LSBs is rough and uneven, with needle-like clusters. In contrast, the Li anode surface of LSBs with Bi_2MoO_6-PPy@PP separator is smooth and uniform, and no obvious peeling or change was observed after cycling at 2 C (Fig. S18). Furthermore, Full XPS profiles show that the surface of the Li anode is primarily composed of polysulfides and sulfates (Fig. S19). The S/Mo element ratio of the Li anode surface of the battery with Bi_2MoO_6-PPy@PP separator after cycling is smaller than that of the PP separator, as shown in Table S3, confirming that Bi_2MoO_6-PPy@PP separator can effectively suppress the shuttle effect.

CONCLUSIONS

In this study, Bi_2MoO_6-PPy nanosheets with a Mott-Schottky heterostructure were used as separator modification layers for LSBs. Bi_2MoO_6-Ppy nanosheets' unique Mott-Schottky heterostructure enables fast electron transfer channels and accelerates polysulfide redox kinetics. Furthermore, with this functional separator, the battery maintains its cycling stability and reversible capacity of up to 596 mA h g^{-1} after more than 500 cycles at a high current density of 2 C. Even at a sulfur content of 7.5 mg cm^{-2}, a high real capacity of 6.3 mA h cm^{-2} is maintained after 80 cycles. Finally, the novel Bi_2MoO_6-PPy Mott-Schottky heterostructure proposed in this work opens up new avenue for developing LSBs.

Received 25 October 2022; accepted 6 December 2022; published online 3 March 2023

1 Wang H, Zhang N, Li Y, *et al.* Unique flexible $NiFe_2O_4$@S/rGO-CNT electrode *via* the synergistic adsorption/electrocatalysis effect toward high-performance lithium-sulfur batteries. J Phys Chem Lett, 2019, 10: 6518–6524
2 Sun C, Sheng J, Zhang Q, *et al.* Self-extinguishing Janus separator with high safety for flexible lithium-sulfur batteries. Sci China Mater, 2022, 65: 2169–2178
3 Hao Z, Chen J, Lu X, *et al.* Precisely visit the performance modulation of functionalized separator in Li-S batteries *via* consecutive multiscale analysis. Energy Storage Mater, 2022, 49: 85–92
4 Zhou C, Li Z, Xu X, *et al.* Metal-organic frameworks enable broad strategies for lithium-sulfur batteries. Natl Sci Rev, 2021, 8: nwab055
5 Yang Y, Meng G, Wang H, *et al.* Efficient polysulfides trapping and redox enabled by Co/N-carbon implanted Li^+-montmorillonite for advanced lithium-sulfur batteries. Chem Eng J, 2023, 451: 138914
6 Yao W, Tian C, Yang C, *et al.* p-doped $NiTe_2$ with Te-vacancies in lithium-sulfur batteries prevents shuttling and promotes polysulfide conversion. Adv Mater, 2022, 34: 2106370
7 Yu B, Chen D, Wang Z, *et al.* Mo_2C quantum dots@graphene functionalized separator toward high-current-density lithium metal anodes for ultrastable Li-S batteries. Chem Eng J, 2020, 399: 125837
8 Mao J, Niu D, Huang G, *et al.* A Ni/Ni_2P heterostructure in modified porous carbon separator for boosting polysulfide catalytic conversion. Sci China Mater, 2022, 65: 2453–2462
9 Yang Y, Mu P, Li B, *et al. In situ* separator modification with an N-rich conjugated microporous polymer for the effective suppression of polysulfide shuttle and Li dendrite growth. ACS Appl Mater Interfaces, 2022, 14: 49224–49232
10 Ma F, Zhang X, Sriniva K, *et al.* NbN nanodot decorated N-doped graphene as a multifunctional interlayer for high-performance lithium-sulfur batteries. J Mater Chem A, 2022, 10: 8578–8590
11 He J, Chen Y, Manthiram A. Vertical Co_9S_8 hollow nanowall arrays grown on a Celgard separator as a multifunctional polysulfide barrier for high-performance Li-S batteries. Energy Environ Sci, 2018, 11: 2560–2568
12 Yang Y, Wang W, Li L, *et al.* Stable cycling of Li-S batteries by simultaneously suppressing Li-dendrite growth and polysulfide shuttling enabled by a bioinspired separator. J Mater Chem A, 2020, 8: 3692–3700
13 Ma F, Srinivas K, Zhang X, *et al.* Mo_2N quantum dots decorated N-doped graphene nanosheets as dual-functional interlayer for dendrite-free and shuttle-free lithium-sulfur batteries. Adv Funct Mater, 2022, 32: 2206113
14 He D, Meng J, Chen X, *et al.* Ultrathin conductive interlayer with high-density antisite defects for advanced lithium-sulfur batteries. Adv Funct Mater, 2020, 31: 2001201
15 Ma F, Yu B, Zhang X, *et al.* $WN_{0.67}$-embedded N-doped graphene-nanosheet interlayer as efficient polysulfide catalyst and absorbant for high-performance lithium-sulfur batteries. Chem Eng J, 2022, 431: 133439
16 Yang Y, Wang W, Meng G, *et al.* Function-directed design of battery separators based on microporous polyolefin membranes. J Mater Chem A, 2022, 10: 14137–14170
17 Tong Z, Huang L, Liu H, *et al.* Defective graphitic carbon nitride modified separators with efficient polysulfide traps and catalytic sites for fast and reliable sulfur electrochemistry. Adv Funct Mater, 2021, 31: 2010455
18 Liu G, Zeng Q, Fan Z, *et al.* Boosting sulfur catalytic kinetics by defect engineering of vanadium disulfide for high-performance lithium-sulfur batteries. Chem Eng J, 2022, 448: 137683
19 Zhang Z, Wang JN, Shao AH, *et al.* Recyclable cobalt-molybdenum bimetallic carbide modified separator boosts the polysulfide adsorption-catalysis of lithium sulfur battery. Sci China Mater, 2020, 63: 2443–2455
20 Jiang Z, Huang Y, Zhu Z, *et al.* Quenching singlet oxygen *via* intersystem crossing for a stable Li-O_2 battery. Proc Natl Acad Sci USA, 2022, 119: e2202835119
21 Zhao T, Chen J, Yuan M, *et al.* Local charge rearrangement to boost the chemical adsorption and catalytic conversion of polysulfides for high-performance lithium-sulfur batteries. J Mater Chem A, 2021, 9: 7566–7574
22 Li F, Kaiser MR, Ma J, *et al.* Free-standing sulfur-polypyrrole cathode in conjunction with polypyrrole-coated separator for flexible Li-S batteries. Energy Storage Mater, 2018, 13: 312–322
23 Li Z, Zhou C, Hua J, *et al.* Engineering oxygen vacancies in a polysulfide-blocking layer with enhanced catalytic ability. Adv Mater, 2020, 32: 1907444
24 Yang T, Liu K, Wu T, *et al.* Rational valence modulation of bimetallic carbide assisted by defect engineering to enhance polysulfide conversion for lithium-sulfur batteries. J Mater Chem A, 2020, 8: 18032–18042
25 Zhu Y, Zuo Y, Ye F, *et al.* Dual-regulation strategy to enhance electrochemical catalysis ability of $NiCo_2O_{4-x}$ for polysulfides conversion in Li-S batteries. Chem Eng J, 2022, 428: 131109
26 Huang S, Wang Y, Hu J, *et al. In situ*-grown compressed $NiCo_2S_4$ barrier layer for efficient and durable polysulfide entrapment. NPG Asia Mater, 2019, 11: 55
27 Zhou C, Chen M, Dong C, *et al.* The continuous efficient conversion and directional deposition of lithium (poly)sulfides enabled by bimetallic site regulation. Nano Energy, 2022, 98: 107332
28 Xiao Y, Guo S, Ouyang Y, *et al.* Constructing heterogeneous structure in metal-organic framework-derived hierarchical sulfur hosts for capturing polysulfides and promoting conversion kinetics. ACS Nano, 2021, 15: 18363–18373
29 Cao Y, Liu C, Wang M, *et al.* Lithiation of covalent organic framework nanosheets facilitating lithium-ion transport in lithium-sulfur batteries. Energy Storage Mater, 2020, 29: 207–215
30 Chen K, Zhang G, Xiao L, *et al.* Polyaniline encapsulated amorphous

V_2O_5 nanowire-modified multi-functional separators for lithium-sulfur batteries. Small Methods, 2021, 5: 2001056
31 Zhang Y, Zhao G, Ge P, *et al.* Bi_2MoO_6 microsphere with double-polyaniline layers toward ultrastable lithium energy storage by reinforced structure. Inorg Chem, 2019, 58: 6410–6421
32 Long B, Qiao Z, Zhang J, *et al.* Polypyrrole-encapsulated amorphous Bi_2S_3 hollow sphere for long life sodium ion batteries and lithium-sulfur batteries. J Mater Chem A, 2019, 7: 11370–11378
33 Zhang L, Wang Z, Hu C, *et al.* Enhanced photocatalytic performance by the synergy of Bi vacancies and Bi_0 in Bi_0-Bi_2-δMoO_6. Appl Catal B-Environ, 2019, 257: 117785
34 Zheng Y, Zhou T, Zhao X, *et al.* Atomic interface engineering and electric-field effect in ultrathin Bi_2MoO_6 nanosheets for superior lithium ion storage. Adv Mater, 2017, 29: 1700396
35 Dong Y, Dong S, Liu B, *et al.* 2D piezoelectric Bi_2MoO_6 nanoribbons for GSH-enhanced sonodynamic therapy. Adv Mater, 2021, 33: 2106838
36 Yim T, Han SH, Park NH, *et al.* Effective polysulfide rejection by dipole-aligned $BaTiO_3$ coated separator in lithium-sulfur batteries. Adv Funct Mater, 2016, 26: 7817–7823
37 Lv X, Lei T, Wang B, *et al.* An efficient separator with low Li-ion diffusion energy barrier resolving feeble conductivity for practical lithium-sulfur batteries. Adv Energy Mater, 2019, 9: 1901800
38 Li Z, Zhang Q, Hencz L, *et al.* Multifunctional cation-vacancy-rich $ZnCo_2O_4$ polysulfide-blocking layer for ultrahigh-loading Li-S battery. Nano Energy, 2021, 89: 106331
39 Qin B, Cai Y, Wang P, *et al.* Crystalline molybdenum carbide-amorphous molybdenum oxide heterostructures: *In situ* surface reconfiguration and electronic states modulation for Li-S batteries. Energy Storage Mater, 2022, 47: 345–353
40 Mao X, Zhu L, Fu A. Arsenene, antimonene and bismuthene as anchoring materials for lithium-sulfur batteries: A computational study. Int J Quantum Chem, 2021, 121: 26661
41 Xu H, Yang S, Li B. Ultrathin bismuth nanosheets as an efficient polysulfide catalyst for high performance lithium-sulfur batteries. J Mater Chem A, 2020, 8: 149–157
42 Sun H, Liu Z, Liu X, *et al.* Preparation and characterization of PPy/Bi_2MoO_6 microspheres with highly photocatalytic performance for removal of highly concentrated organic dyes. Mater Today Sustain, 2022, 19: 100154
43 Xie R, Fan J, Fang K, *et al.* Hierarchical Bi_2MoO_6 microsphere photocatalysts modified with polypyrrole conjugated polymer for efficient decontamination of organic pollutants. Chemosphere, 2022, 286: 131541
44 Yuan S, Zhao Y, Chen W, *et al.* Self-assembled 3D hierarchical porous Bi_2MoO_6 microspheres toward high capacity and ultra-long-life anode material for Li-ion batteries. ACS Appl Mater Interfaces, 2017, 9: 21781–21790
45 Shetty M, Murthy M, Shastri M, *et al.* Hydrothermally synthesized Bi_2MoO_6/reduced graphene oxide composite as anodes for lithium-ion batteries. Ceramics Int, 2019, 45: 24965–24970
46 Zhai X, Gao J, Xue R, *et al.* Facile synthesis of Bi_2MoO_6/reduced graphene oxide composites as anode materials towards enhanced lithium storage performance. J Colloid Interface Sci, 2018, 518: 242–251
47 Zhang P, Wang D, Zhu Q, *et al.* Plate-to-layer Bi_2MoO_6/MXene-heterostructured anode for lithium-ion batteries. Nano-Micro Lett, 2019, 11: 81
48 Li Y, Wang W, Liu X, *et al.* Engineering stable electrode-separator interfaces with ultrathin conductive polymer layer for high-energy-density Li-S batteries. Energy Storage Mater, 2019, 23: 261–268
49 Wang Y, He L, Dang G, *et al.* Polypyrrole-functionalized magnetic Bi_2MoO_6 nanocomposites as a fast, efficient and reusable adsorbent for removal of ketoprofen and indomethacin from aqueous solution. J Colloid Interface Sci, 2021, 592: 51–65
50 Hussain SK, Dudem B, Yu JS. Enhanced electrochemical performance *via* PPy encapsulated 3D flower-like bismuth molybdate nanoplates for high-performance supercapacitors. Appl Surf Sci, 2019, 478: 846–856
51 Dong Y, Liu Y, Hu Y, *et al.* Boosting reaction kinetics and reversibility in Mott-Schottky VS_2/MoS_2 heterojunctions for enhanced lithium storage. Sci Bull, 2020, 65: 1470–1478
52 Li Y, Wang W, Zhang B, *et al.* Manipulating redox kinetics of sulfur species using Mott-Schottky electrocatalysts for advanced lithium-sulfur batteries. Nano Lett, 2021, 21: 6656–6663
53 Zhang D, Luo Y, Liu J, *et al.* $ZnFe_2O_4$-Ni_5P_4 Mott-Schottky heterojunctions to promote kinetics for advanced Li-S batteries. ACS Appl Mater Interfaces, 2022, 14: 23546–23557
54 Wang Y, Zhang R, Sun Z, *et al.* Spontaneously formed Mott-Schottky electrocatalyst for lithium-sulfur batteries. Adv Mater Interfaces, 2020, 7: 1902092
55 Shi M, Liu Z, Zhang S, *et al.* A Mott-Schottky heterogeneous layer for Li-S batteries: Enabling both high stability and commercial-sulfur utilization. Adv Energy Mater, 2022, 12: 2103657
56 Zhang C, Du R, Biendicho JJ, *et al.* Tubular CoFeP@CN as a Mott-Schottky catalyst with multiple adsorption sites for robust lithium-sulfur batteries. Adv Energy Mater, 2021, 11: 2100432
57 Li H, Chen H, Chen Y, *et al.* Enhancing the bidirectional reaction kinetics of polysulfides by Mott-Schottky-like electrocatalysts with rich heterointerfaces. ACS Sustain Chem Eng, 2022, 10: 5092–5100

Acknowledgements This work was supported by Hainan Provincial Joint Project of Sanya Yazhou Bay Science and Technology City (520LH056), and the National Key Research and Development Program of China (2022YFB3803502).

Author contributions Gu J conceived the proposal, synthesized the materials and wrote the manuscript. Dong C measured the battery performance. Zhou C carried out the theoretical calculations. Shen C performed XPS and SEM characterizations of the materials. Pi Y and Xu X contributed resources and supervised the project. All authors contributed to the general discussion.

Conflict of interest The authors declare that they have no conflict of interest.

Supplementary information Supporting data are available in the online version of the paper.

Jiapei Gu earned her MS from the South China Normal University in 2021. She is a PhD candidate in materials science and engineering at Wuhan University of Technology (WUT). Her current research focuses on developing novel nanomaterials and structures for lithium-sulfur batteries.

Yuqiang Pi earned his PhD in materials science from WUT in 2021 and is now employed by Hubei Engineering University. His current research focuses primarily on electrochemical energy storage devices such as lithium-sulfur batteries, lithium-ion batteries, sodium-ion batteries, and aqueous Fe-ion batteries.

Xu Xu is an associate professor at International School of Materials Science and Engineering, WUT. He earned his PhD in materials science from WUT and worked as a visiting graduate researcher at the University of California, Los Angeles. His current research interests are primarily in energy storage materials and devices, such as lithium-sulfur batteries, lithium metal batteries, and thin film batteries.

具有协同吸附-催化效应的莫特-肖特基异质结构修饰隔膜助力锂硫电池

谷佳佩[1], 冬晨旭[1], 周铖[1], 沈春丽[1], 皮玉强[2*], 许絮[1*]

摘要 锂硫电池(LSBs)的实际应用受到硫利用率低、严重的穿梭效应和缓慢的氧化还原反应的限制. 本工作通过使用新型莫特-肖特基异质结构对隔膜进行改性的策略有效地缓解上述问题. 具体而言, 这种特殊结构通过导电聚合物聚吡咯(PPy)在Bi_2MoO_6纳米片表面原位聚合形成Bi_2MoO_6-PPy纳米片来合成. 基于Bi_2MoO_6-PPy纳米片的强吸附效应、高催化活性和内置电场, 这种新型异质结构可以降低多硫化物上的氧化还原能垒. 使用由Bi_2MoO_6-PPy纳米片改性的功能隔膜组装的电池显示出良好的循环稳定性, 在2 C下500次循环中, 每次循环的容量衰减低至0.045%. 此外, 即使在高硫负载(7.5 mg cm^{-2})下, 电池在80次循环后仍显示出6.3 mA h cm^{-2}的面积容量. 因此, Bi_2MoO_6-PPy纳米片改性隔膜(Bi_2MoO_6-PPy@PP隔膜)有效地抑制了穿梭效应, 为锂硫电池高效催化剂的应用提供了有效策略.